LETTERS

Phase diagram of a two-component Fermi gas with resonant interactions

Yong-il Shin[1], Christian H. Schunck[1], André Schirotzek[1] & Wolfgang Ketterle[1]

The pairing of fermions lies at the heart of superconductivity and superfluidity. The stability of these pairs determines the robustness of the superfluid state, and the quest for superconductors with high critical temperature equates to a search for systems with strong pairing mechanisms. Ultracold atomic Fermi gases present a highly controllable model system for studying strongly interacting fermions[1]. Tunable interactions (through Feshbach collisional resonances) and the control of population or mass imbalance among the spin components provide unique opportunities to investigate the stability of pairing[2–4]—and possibly to search for exotic forms of superfluidity[5,6]. A major controversy has surrounded the stability of superfluidity against an imbalance between the two spin components when the fermions interact resonantly (that is, at unitarity). Here we present the phase diagram of a spin-polarized Fermi gas of ^{6}Li atoms at unitarity, experimentally mapping out the superfluid phases versus temperature and density imbalance. Using tomographic techniques, we reveal spatial discontinuities in the spin polarization; this is the signature of a first-order superfluid-to-normal phase transition, and disappears at a tricritical point where the nature of the phase transition changes from first-order to second-order. At zero temperature, there is a quantum phase transition from a fully paired superfluid to a partially polarized normal gas. These observations and the implementation of an *in situ* ideal gas thermometer provide quantitative tests of theoretical calculations on the stability of resonant superfluidity.

When the two spin components resonantly interact, the behaviour of the system becomes independent of the nature of the interactions. This case of unitarity has become a benchmark for experimental and theoretical studies over the last few years. However, there is an ongoing debate about the stability of resonant superfluidity, reflected in major discrepancies in predicted transition temperatures for the balanced spin mixture[7–9], and an even more dramatic discrepancy for the critical imbalance of the two spin components, called the Chandrasekhar–Clogston limit of superfluidity[2,3]. Recent quantum Monte Carlo calculations predicted that superfluidity would be quenched by a density imbalance around 40% (ref. 10), whereas other studies predicted a critical imbalance above 90% (refs 11–16). Our earlier work[17–19] suggested the lower limit but other experiments[20,21] were interpreted to be consistent with the absence of the Chandrasekhar–Clogston limit. This huge discrepancy reveals that even qualitative aspects, such as the role of interactions in the normal phase, are still controversial. The lack of reliable thermometry for strongly interacting systems limits the full interpretations of experimental results.

Here we resolve this long-standing debate by presenting the phase diagram of a spin-polarized Fermi gas at unitarity. We observe that the normal-to-superfluid phase transition changes its nature. At low temperature, the phase transition occurs with a jump in the spin polarization as the imbalance increases, which we interpret as a first-order phase transition. The local spin polarization or local density imbalance is defined as $\sigma = (n_\uparrow - n_\downarrow)/(n_\uparrow + n_\downarrow)$, where $\uparrow$ and $\downarrow$ refer to the two spin components with densities $n_{\uparrow,\downarrow}$. At high temperature, the phase transition is smooth and therefore of second order. The two regimes are connected by a tricritical point[4,22] and we estimate its position to be $(\sigma_{tc}, T_{tc}/T_{F\uparrow}) \approx (0.2, 0.07)$, where $k_B T_{F\uparrow} = \hbar^2(6\pi^2 n_\uparrow)^{2/3}/2m$ is the Fermi energy of the majority component of density $n_\uparrow$ (k_B is the Boltzmann constant, $\hbar$ is the Planck constant divided by 2π and m is the atomic mass of ^{6}Li). Our low-temperature results confirm a zero-temperature quantum phase transition at a critical polarization $\sigma_{c0} \approx 36\%$.

This work required the introduction of several techniques. A tomographic reconstruction of local Fermi temperatures and spin polarization allowed us to obtain the phase diagram for the homogeneous system, no longer affected by the inhomogeneous density of the trapped samples. Furthermore, absolute temperatures were obtained using *in situ* thermometry applied to the non-interacting fully polarized Fermi gas in the outer part of the trapped samples, an ideal thermometer with exactly known thermal properties. Unlike previous work[18,23], this is a direct measurement without any approximations.

Our experiments are carried out in a trapping potential $V(\mathbf{r})$. The local chemical potential of each spin component is given as $\mu_{\uparrow,\downarrow}(\mathbf{r}) = \mu_{\uparrow 0,\downarrow 0} - V(\mathbf{r})$, where $\mu_{\uparrow 0,\downarrow 0}$ are the global chemical potentials. When $\mu_{\uparrow 0} \neq \mu_{\downarrow 0}$, owing to imbalanced populations, the chemical potential ratio $\eta(\mathbf{r}) = \mu_\downarrow/\mu_\uparrow$ varies spatially over the trapped sample and so, under the local density approximation, the trapped inhomogeneous sample is represented by a line in the phase diagrams of the homogeneous system. Figure 1 illustrates the spatial structure of a strongly interacting Fermi mixture in a harmonic trap. In the inner region, where η is closer to unity, a superfluid with zero (or small) spin polarization will form at zero (or low) temperatures, having a sharp phase boundary against the partially polarized normal gas in the outer region. The spin polarization shows a discontinuity at the boundary of the superfluid core at $r = R_c$, a signature of the phase separation of a superfluid and a normal gas[24]. The critical polarization $\sigma_c = \lim_{r \to R_c^+} \sigma(r)$ represents the minimum spin polarization for a stable normal gas; $\sigma_s = \lim_{r \to R_c^-} \sigma(r)$ represents the maximum spin polarization for a stable superfluid gas. At higher temperatures, the discontinuity in the density imbalance disappears. The main result of this paper is the observation and quantitative analysis of such density profiles. Because we have no experimental evidence, we are not discussing the exotic partially polarized phases[25] which could exist only in the transition layer between the superfluid core and the normal outer region.

We prepared a variable spin mixture of the two lowest hyperfine states of ^{6}Li atoms, labelled $|\uparrow\rangle$ and $|\downarrow\rangle$, at a magnetic field of 833 G. A

[1]Department of Physics, MIT-Harvard Center for Ultracold Atoms, and Research Laboratory of Electronics, MIT, Cambridge, Massachusetts, 02139, USA.

broad Feshbach resonance at 834 G enhances the interactions between the two spin states. Our sample was confined in a three-dimensional harmonic trap with cylindrical symmetry. The *in situ* density distributions of the majority (spin ↑) and minority (spin ↓) components were determined using a phase-contrast imaging technique[19] (Fig. 2). We obtained the low-noise profiles $\tilde{n}$ by averaging the column density distribution along the equipotential line and determined the three-dimensional density profiles $n(r)$ using the inverse Abel transformation of the column densities $\tilde{n}(r)$ (see Methods Summary). Most of our measurements were performed at a total population imbalance of $\delta \approx 50\%$, where $\delta = (N_\uparrow - N_\downarrow)/(N_\uparrow + N_\downarrow)$ refers to the total numbers of atoms in the sample, $N_\uparrow$ and $N_\downarrow$ of the spin ↑ and ↓ components, respectively.

Figure 3 displays the radial profiles of the densities $n_{\uparrow,\downarrow}(r)$ and the corresponding spin polarization $\sigma(r)$ for various temperatures. The discontinuity in the spin polarization, clearly shown at very low temperatures, demonstrates the phase separation of the inner superfluid of low polarization and the outer normal gas of high polarization. At low temperature, the core radius R_c is determined as the kink (and/or peak) position in the column density difference profile. At high temperature (but still in the superfluid regime), the discontinuity in $\sigma(r)$ disappears. At our lowest temperature, the radii of the minority cloud and the core region were measured as $R_\downarrow = 0.73(1)R_\uparrow$ and $R_c = 0.430(3)R_\uparrow$ (at $\delta = 44(4)\%$), respectively, and these values agree with recent theoretical calculations[10,25] within the experimental uncertainties due to the determination of δ. Here, $R_\uparrow$ is the radius of the majority cloud, and the uncertainty of the final digit is indicated by parentheses.

We determined temperature from the *in situ* majority wing profiles. The outer part of the majority component, forming a non-interacting Fermi gas, fulfils the definition of an ideal thermometer, namely a substance with exactly understood properties in contact with the target sample. This new *in situ* method avoids the modification of the ideal gas profile caused by the collision with the inner core during ballistic expansion (ref. 18, see Supplementary Information). The outer part of the averaged column density difference profile ($r > R_\downarrow$) was fitted to a finite temperature Fermi–Dirac distribution in a harmonic trap (Fig. 4) and the relative temperature $T' \equiv T/T_{F0}$ was determined, where $k_B T_{F0} = \hbar^2(6\pi^2 n_0)^{2/3}/2m$ is the Fermi energy of the non-interacting Fermi gas, which has the same density distribution in the outer region as the majority cloud (n_0 is the central density of the non-interacting Fermi gas at zero temperature). We verified that anharmonicity of the trapping potential does not affect the fitted temperature (see Methods).

The critical lines of the phase diagram of a homogeneous spin-polarized Fermi gas were obtained by determining the local temperature and spin polarization at the phase boundary. The local relative temperature $T'_{local} \equiv T/T_{F\uparrow}$ was derived from the local density $n_\uparrow(R_c)$ according to $T'(R_c) = T/T_{F0} \times (n_0/n_\uparrow(R_c))^{2/3}$. Because we observe no jump in the majority density within our resolution, $T_{F\uparrow}$ is well-defined at the boundary. The critical polarizations σ_c and σ_s were measured as $\sigma_c = \sigma(R_c)$ and $\sigma_s = \sigma(R_c - 0.05R_\uparrow)$ (this criterion for σ_s was more robust than a fitting procedure, but excludes the possibility that σ_s will be equal to σ_c at high temperature. Therefore, the measured σ_s should be regarded as a lower bound for the polarization of

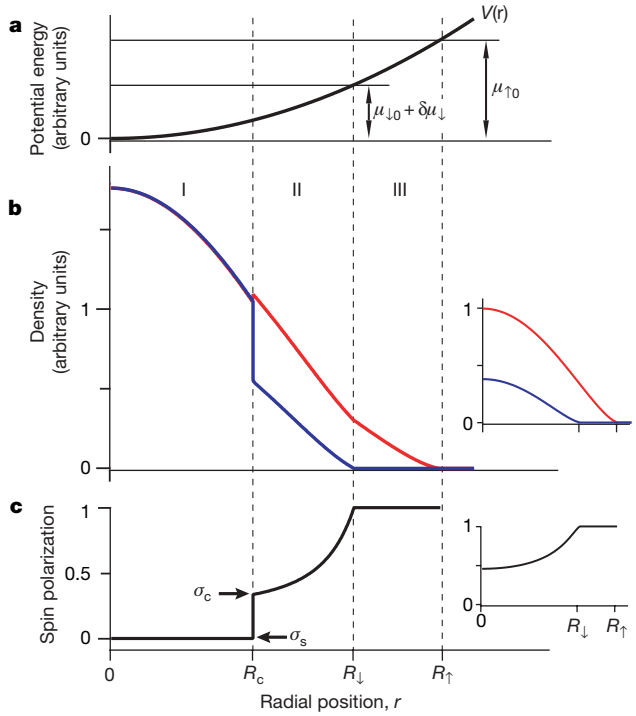

Figure 1 | Schematic of spatial structure of a strongly interacting Fermi gas in a harmonic trap. **a**, A two-component (spin ↑ and ↓) Fermi mixture is confined in an external potential $V(r) \propto r^2$ with the chemical potential $\mu_{\uparrow 0,\downarrow 0}$ of each spin component ($\delta\mu_\downarrow$ is the shift for the spin ↓ component owing to interactions). **b**, Density distributions of the majority component $n_\uparrow(r)$ (red line) and the minority component $n_\downarrow(r)$ (blue line). **c**, Spin polarization $\sigma(r) = (n_\uparrow - n_\downarrow)/(n_\uparrow + n_\downarrow)$. At zero temperature, the sample has a three-layer radial structure: (I), the core region ($0 \le r < R_c$) of a fully paired superfluid with $n_\uparrow = n_\downarrow$; (II), the intermediate region ($R_c < r < R_\downarrow$) of a partially polarized normal gas; and (III), the outer region ($R_\downarrow < r < R_\uparrow$) of a fully polarized normal gas. The critical polarization σ_c (or σ_s) is defined as the minimum (or maximum) spin polarization of the normal (or superfluid) region. The non-interacting case is shown in the insets. The insets have the same axes as the main figure.

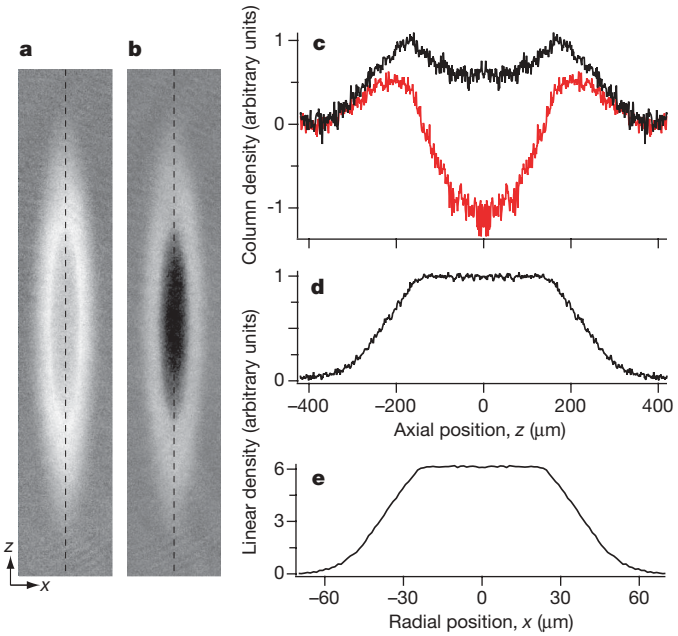

Figure 2 | Double *in situ* phase-contrast imaging of a trapped Fermi mixture. Two phase-contrast images of one sample were taken using different probe frequencies of the imaging beam, measuring the density difference $n_{d1} = n_\uparrow - n_\downarrow$ (**a**) and the weighted density difference $n_{d2} = 0.76n_\uparrow - 1.43n_\downarrow$ (**b**), respectively. The images show the two-dimensional distribution of the column density difference, $\tilde{n}_{d1,2}(x,z) \equiv \int n_{d1,2}(\mathbf{r})\mathrm{d}y$, owing to the line-of-sight integration. The field of view for each image is 150 μm × 820 μm. **c**, The distributions of the column density difference $\tilde{n}_{d1}$ (black line) and $\tilde{n}_{d2}$ (red line) along the central line (the dashed lines in **a** and **b**). The profiles of the integrated linear density difference, $\bar{n}_{d1,z} \equiv \int \tilde{n}_{d1}(x,z)\mathrm{d}x$ (**d**) and $\bar{n}_{d1,x} \equiv \int \tilde{n}_{d1}(x,z)\mathrm{d}z$ (**e**), show the identical flat-top feature except scaling. The aspect ratio of the trapping potential was $\lambda = 6.15$, the majority atom number was $N_\uparrow = 5.9(5) \times 10^6$, the population imbalance was $\delta = 44(4)\%$, and the relative temperature was $T' = T/T_{F0} = 0.03(1)$ (see text for definitions).

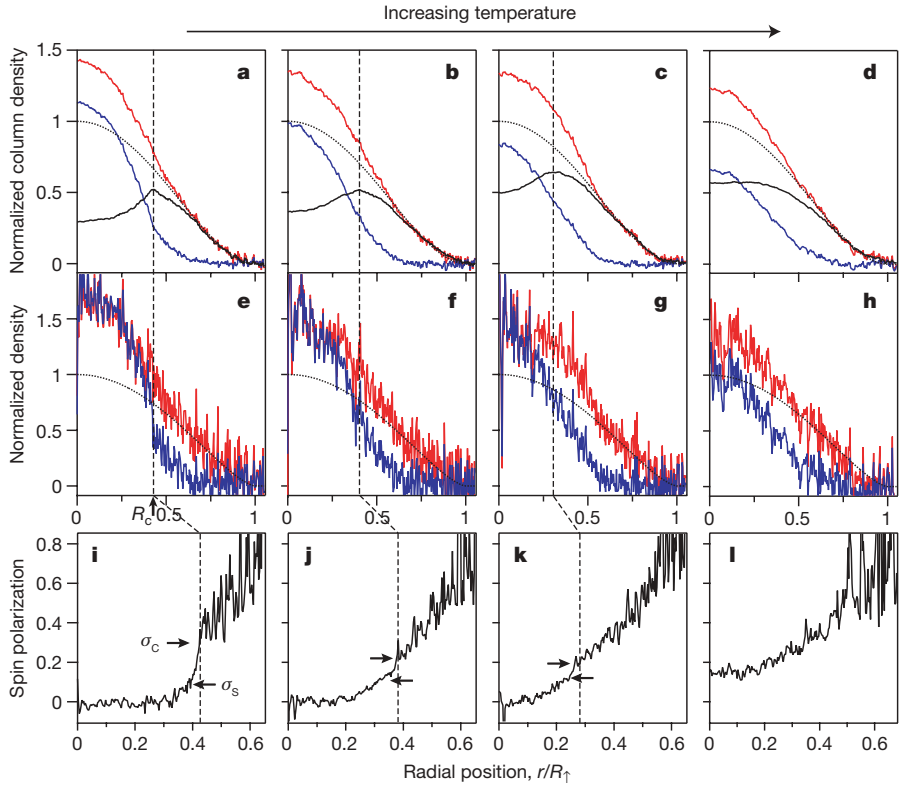

Figure 3 | Density profiles of trapped Fermi mixtures with imbalanced populations. The top row (**a**–**d**) shows the averaged column density profiles for various temperatures (red, majority; blue, minority; black, difference). The majority radius $R_\uparrow$ was determined from the outer region ($r > R_\downarrow$, where $R_\downarrow$ is the radius of the minority cloud) of the majority profiles using a fit to a zero-temperature Thomas–Fermi distribution (black dotted lines). The column densities are normalized by the central value of the fitted Thomas–Fermi distribution. The middle row (**e**–**h**) and the bottom row (**i**–**l**) show the reconstructed three-dimensional profiles and the spin polarization profiles $\sigma(r)$ corresponding to the profiles in **a**–**d**. The core radius R_c was determined as the peak (and/or kink) position in the column density difference (only for **a**–**c**), indicated by the vertical dashed lines. The two spin polarizations σ_c at $r = R_c$ and σ_s at $r = R_c - 0.05R_\uparrow$ are marked by the right and left arrows, respectively. The values for T', σ_c, $R_c/R_\uparrow$, $R_\uparrow$ (in μm), $N_\uparrow$, δ (in %) and λ were, respectively: for **a**, **e** and **i**, 0.03(1), 0.34, 0.43, 385, $5.9(5) \times 10^6$, 44(4), 6.15; for **b**, **f** and **j**, 0.05(2), 0.24, 0.39, 416, $1.0(1) \times 10^7$, 48(4), 6.5; for **c**, **g** and **k**, 0.07(1), 0.21, 0.29, 443, $1.2(2) \times 10^7$, 54(4), 6.5; for **d**, **h** and **l**, 0.10(1), not determined, not determined ($\sigma_{r=0} = 0.15$ and condensate fraction = 2(1)%), 398, $5.3(4) \times 10^6$, 54(4), 7.7.

the superfluid at the boundary). The discontinuity in the spin polarization profile implies that there is a thermodynamically unstable window, $\sigma_s < \sigma < \sigma_c$, leading to a first-order superfluid-to-normal phase transition. As the temperature increases, the unstable region reduces with decreasing σ_c and increasing σ_s. For high temperature when the bimodal feature in the spin polarization profile disappears, we recorded the condensate fraction as an indicator of superfluidity, using the rapid field-ramp technique[17]. As the temperature decreases, the condensate fraction gradually increases with a finite central polarization[19]. Such smooth variations of the density profile and condensate fraction across the phase transition are characteristic of a second-order phase transition.

The phase diagram is characterized by three distinct points: the critical temperature T_{c0} for a balanced mixture, the critical polarization σ_{c0} of a normal gas at zero temperature, and the tricritical point (σ_{tc}, T_{tc}) at which the nature of the phase transition changes. Owing to the lack of a predicted functional form for the phase transition line in the σ–T plane, we apply a linear fit to the measured critical points, suggesting $T_{c0}/T_{F\uparrow} \approx 0.15$, $\sigma_{c0} \approx 0.36$ and $(\sigma_{tc}, T_{tc}/T_{F\uparrow}) \approx (0.20, 0.07)$. The value for σ_{c0} agrees well with the prediction (from the quantum Monte Carlo calculation) of 0.39 (ref. 10). The extrapolation of the phase diagram to $\sigma = 0$ is tentative, because the *in situ* thermometry could not be applied to small population imbalances owing to the narrowness of the non-interacting outer region.

The Chandrasekhar–Clogston limit reflects the energetic competition between a superfluid state and a partially polarized normal state, and occurs at a critical value of $2h_c$ for the chemical potential difference $\delta\mu = \mu_\uparrow - \mu_\downarrow$. In Bardeen–Cooper–Schrieffer theory, which is valid for weak interactions, $h_c = \Delta/\sqrt{2}$ (ref. 3). Here, Δ is the pairing gap. With the assumption of no interactions in a normal gas, quantum Monte Carlo studies predict $h_c = 1.00(5)\Delta \approx 1.2\mu$ at unitarity[11], where $\mu = (\mu_\uparrow + \mu_\downarrow)/2$. The condition $\mu_{\downarrow c} = \mu - h_c < 0$ requires $n_\downarrow = 0$ for a non-interacting normal gas, implying the absence of a partially polarized normal phase and consequently $\sigma_{c0} = 100\%$. Mean-field approaches[12–16], which cannot treat the interactions in the normal phase accurately, also predict a high critical imbalance $\sigma_{c0} > 90\%$. Strong interactions in the normal phase, however, have been observed through the compressed shape of the minority cloud[18] and the shift in the radio frequency excitation spectrum[26]. The data in Fig. 5 clearly establish a zero-temperature Chandrasekhar–Clogston limit for σ_{c0} in the range 30% to 40%. By analysing the *in situ* density profiles[25,27], we obtained $h_c \approx 0.95\mu$ (see Methods). Since theory clearly predicts $\mu < \Delta$ at unitarity[9,11], we have $h_c < \Delta$. If h_c were larger than Δ, polarized quasi-particles would have negative energies and would already form at zero temperature. Therefore, up to our observed value of h_c, the fully paired

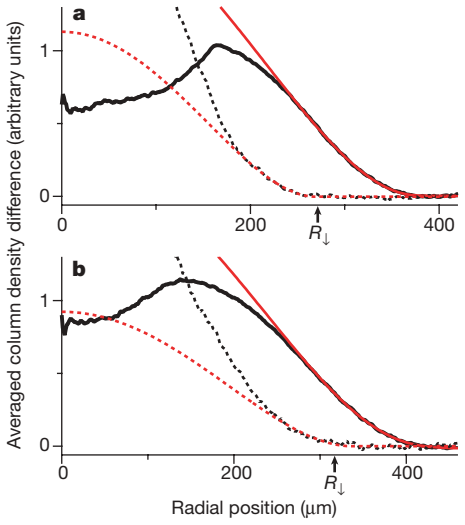

Figure 4 | Temperature determination using *in situ* density profiles. The relative temperature $T' = T/T_{F0}$ (see text for definition) was determined from the outer region ($r > R_\downarrow$) of the averaged column density difference profile (black line) fitted to a finite temperature Fermi–Dirac distribution (red line). The radius of the minority cloud $R_\downarrow$ was determined from a fit of the wing profile of the minority component (black dashed line) to a zero-temperature Thomas–Fermi distribution (red dashed line). **a**, $T' = 0.03(1)$ and $\delta = 44(4)\%$. **b**, $T' = 0.08(1)$ and $\delta = 46(4)\%$.

superfluid state is stable, and a polarized superfluid exists only at finite temperature.

The interface between two immiscible fluids involves a surface energy, leading to at least a small violation of the local density approximation. However, the observed sharp interface along an equipotential line and the flat-top structure of the linear density difference profiles (Fig. 2d and e) imply that corrections to the local density approximation are smaller than the resolution of our experiment. These observations are inconsistent with the interpretations given for the experimental results reported in refs 20 and 21, where it has been shown that highly elongated small samples are deformed by surface tension[28,29]. The scaling of those surface effects to our parameters predicted a deviation of the aspect ratio of the superfluid core of about 15% from the trap aspect ratio[29], whereas our data gives an upper bound of 2%. We note that surface tension would add energy in the phase-separated superfluid regime and would shift the Chandrasekhar–Clogston limit to smaller values. Refs 20 and 21 concluded that the Chandrasekhar–Clogston limit should be $\delta_{c0} > 95\%$, which is ruled out by our observations. We are not aware of any suggested effect that can reconcile the data of refs 20 and 21 with our phase diagram for a resonant superfluid. To identify this finite size effect and to understand fully the nature of the normal state[26], more work on imbalanced Fermi gases is needed.

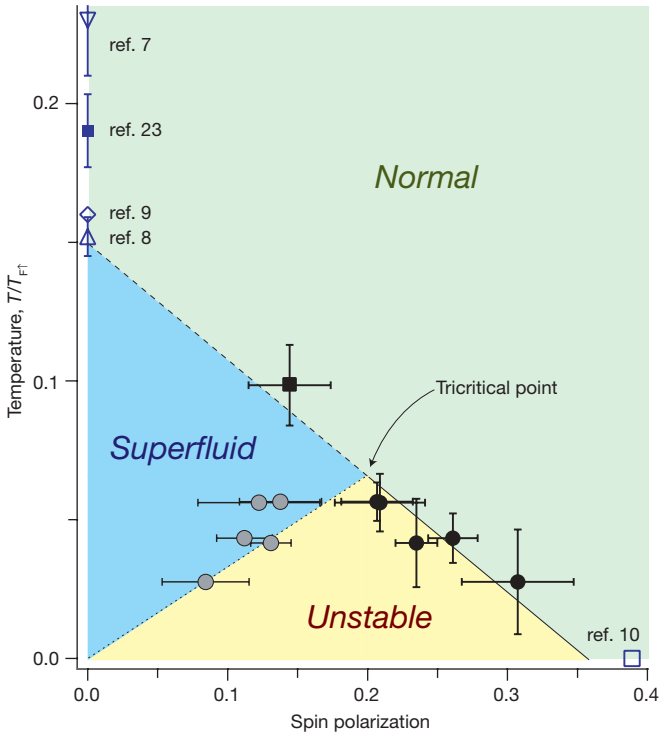

Figure 5 | The σ–T phase diagram for a homogeneous spin-polarized Fermi gas with resonant interactions. The critical polarizations σ_c (black solid circles and square) and σ_s (grey solid circles) are displayed along the local $T/T_{F\uparrow}$ at the phase boundary. The yellow area ($\sigma_s < \sigma < \sigma_c$) represents a thermodynamically unstable region, leading to the phase separation. Above the tricritical point, the phase transition in the centre of the cloud was observed by the onset of pair condensation. For this, a cloud was evaporatively cooled, until it crossed the phase transition on a trajectory almost perpendicular to the phase transition line (see Supplementary Information). The critical spin polarization and temperature were obtained by interpolating between points without and with small condensates (black solid square). The linear fit to the σ_c values is shown as a guide to the eye for the normal-to-superfluid phase transition line. Each data point consists of five independent measurements and error bars indicate standard deviation. The blue open symbols show theoretical predictions for the critical temperature of a homogeneous equal mixture[7–9] and the critical polarization at zero temperature[10]. The blue solid square is the measured critical temperature of ref. 23, multiplied by $\sqrt{\xi}$ with $\xi = 0.42$ (ref. 11) to obtain local T/T_F at the centre. Finite temperature correction may increase the effective value of ξ.

In conclusion, we have established the phase diagram of a homogeneous spin-polarized Fermi gas with resonant interactions in the σ–T plane. This includes the identification of a tricritical point at which the critical lines for first-order and second-order phase transitions meet, and the final confirmation of a zero-temperature quantum phase transition—the Chandrasekhar–Clogston limit of superfluidity—for a gas at unitarity. So far, predicted exotic superfluid states such as the breached-pair state in a stronger coupling regime (Bose–Einstein condensate side)[13] and the Fulde–Ferrell–Larkin–Ovchinnikov state in a weaker coupling regime (Bardeen–Cooper–Schrieffer side)[5,6,12,16,30] have not been observed, but the novel methods of tomography and thermometry will be important tools in the search for those states.

METHODS SUMMARY

The experimental procedure has been described in our previous publications[17–19]. A degenerate Fermi gas of ^{6}Li atoms was first prepared in an optical trap, using laser cooling and sympathetic cooling with ^{23}Na atoms. A variable spin mixture of the two lowest hyperfine states $|\uparrow\rangle$ and $|\downarrow\rangle$ (corresponding to the $|F=1/2,\ m_F=1/2\rangle$ and $|F=1/2,\ m_F=-1/2\rangle$ states at low magnetic field) was created at a magnetic field $B = 885$ G. The final evaporative cooling was achieved by lowering the trap depth and all measurements were performed at $B = 833$ G. The temperature of the cloud was controlled by the lowest value of the trap depth in the evaporative cooling process. The oscillation frequency in the axial direction was $f_z = 23$ Hz. The two transverse oscillation frequencies f_ρ are equal to within less than 2%. Two phase-contrast images of the same sample were taken consecutively with different probe frequencies, ν_1 and ν_2 (Fig. 2). The time interval between the two images was 10 μs, and the pulse duration of each probe beam was 15 μs. Because the probe beam was off-resonant, no heating effect of the first pulse was observed in the second image. The trapped sample was observed to have an elliptical shell structure of the same aspect ratio $\lambda = f_\rho/f_z$ as the trapping potential over our entire temperature range, and we obtained the low-noise profiles $\tilde{n}$ by averaging the column density distribution along the equipotential line defined as $\lambda^2x^2 + z^2 = r^2$ for a given radial position r. The region for averaging was restricted depending on the type of analysis. Deviations from the trap aspect ratio were only found for the outer thermal wings. Details of the phase-contrast imaging technique and the data analysis are given in Methods and Supplementary Information.

Full Methods and any associated references are available in the online version of the paper at www.nature.com/nature.

Received 19 September; accepted 8 November 2007.

1. Giorgini, S., Pitaevskii, L. P. & Stringari, S. Theory of ultracold Fermi gases. Preprint at ⟨http://arxiv.org/abs/0706.3360⟩ (2007).
2. Chandrasekhar, B. S. A note on the maximum critical field of high-field superconductors. *Appl. Phys. Lett.* **1**, 7–8 (1962).
3. Clogston, A. M. Upper limit for the critical field in hard superconductors. *Phys. Rev. Lett.* **9**, 266–267 (1962).
4. Sarma, G. On the influence of a uniform exchange field acting on the spins of the conduction electrons in a superconductor. *J. Phys. Chem. Solids* **20**, 1029–1032 (1963).
5. Fulde, P. & Ferrell, R. A. Superconductivity in a strong spin-exchange field. *Phys. Rev.* **135**, A550–A563 (1964).
6. Larkin, A. I. & Ovchinnikov, Y. N. Inhomogeneous state of superconductors. *Sov. Phys. JETP* **20**, 762–769 (1965).
7. Bulgac, A., Drut, J. E. & Magierski, P. Spin 1/2 fermions in the unitary regime: a superfluid of a new type. *Phys. Rev. Lett.* **96**, 090404 (2006).
8. Burovski, E., Prokofev, N., Svistunov, B. & Troyer, M. Critical temperature and thermodynamics of attractive fermions at unitarity. *Phys. Rev. Lett.* **96**, 160402 (2006).
9. Haussmann, R., Rantner, W., Cerrito, S. & Zwerger, W. Thermodynamics of the BCS-BEC crossover. *Phys. Rev. A.* **75**, 023610 (2007).
10. Lobo, C., Recati, A., Giorgini, S. & Stringari, S. Normal state of a polarized Fermi gas at unitarity. *Phys. Rev. Lett.* **97**, 200403 (2006).
11. Carlson, J. & Reddy, S. Asymmetric two-component fermion systems in strong coupling. *Phys. Rev. Lett.* **95**, 060401 (2005).
12. Sheehy, D. E. & Radzihovsky, L. BEC-BCS Crossover in "magnetized" Feshbach-resonantly paired superfluids. *Phys. Rev. Lett.* **96**, 060401 (2006).
13. Yi, W. & Duan, L.-M. Phase diagram of a polarized Fermi gas across a Feshbach resonance in a potential trap. *Phys. Rev. A* **74**, 013610 (2006).
14. Gubbels, K. B., Romans, M. W. & Stoof, H. T. Sarma phase in trapped unbalanced Fermi gases. *Phys. Rev. Lett.* **97**, 210402 (2006).

15. Chien, C.-C., Chen, Q., He, Y. & Levin, K. Superfluid phase diagrams of trapped Fermi gases with population imbalance. *Phys. Rev. Lett.* **98,** 110404 (2007).
16. Parish, M. M., Marchetti, F. M., Lamacraft, A. & Simons, B. D. Finite-temperature phase diagram of a polarized Fermi condensate. *Nature Phys.* **3,** 124–128 (2007).
17. Zwierlein, M. W., Schirotzek, A., Schunck, C. H. & Ketterle, W. Fermionic superfluidity with imbalanced spin populations. *Science* **311,** 492–496 (2006).
18. Zwierlein, M. W., Schunck, C. H., Schirotzek, A. & Ketterle, W. Direct Observation of the superfluid phase transition in ultracold Fermi gases. *Nature* **442,** 54–58 (2006).
19. Shin, Y., Zwierlein, M. W., Schunck, C. H., Schirotzek, A. & Ketterle, W. Observation of phase separation in a strongly interacting imbalanced Fermi gas. *Phys. Rev. Lett.* **97,** 030401 (2006).
20. Partridge, G. B., Li, W., Karmar, R. I., Liao, Y. & Hulet, R. G. Pairing and phase separation in a polarized Fermi gas. *Science* **311,** 503–505 (2006).
21. Partridge, G. B., Li, W., Karmar, R. I., Liao, Y. & Hulet, R. G. Deformation of a trapped Fermi gas with unequal spin populations. *Phys. Rev. Lett.* **97,** 190407 (2006).
22. Griffiths, R. B. Thermodynamics near the two-fluid critical mixing point in He^3-He^4. *Phys. Rev. Lett.* **24,** 715–717 (1970).
23. Luo, L., Clancy, B., Joseph, J., Kinast, J. & Thomas, J. E. Measurement of the entropy and critical temperature of a strongly interacting Fermi gas. *Phys. Rev. Lett.* **98,** 080402 (2007).
24. Bedaque, P. F., Caldas, H. & Rupak, G. Phase separation in asymmetrical fermion superfluids. *Phys. Rev. Lett.* **91,** 247002 (2003).
25. Bulgac, A. & Forbes, M. M. Zero-temperature thermodynamics of asymmetric Fermi gases at unitarity. *Phys. Rev. A* **75,** 031605(R) (2007).
26. Schunck, C. H., Shin, Y., Schirotzek, A., Zwierlein, M. W. & Ketterle, W. Pairing without superfluidity: the ground state of an imbalanced Fermi mixture. *Science* **316,** 867–870 (2007).
27. Chevy, F. Universal phase diagram of a strongly interacting Fermi gas with unbalanced spin populations. *Phys. Rev. A* **74,** 063628 (2006).
28. De Silva, T. N. & Mueller, E. J. Surface tension in unitary Fermi gases with population imbalance. *Phys. Rev. Lett.* **97,** 070402 (2006).
29. Haque, M. & Stoof, H. T. C. Trapped fermionic clouds distorted from the trap shape due to many-body effects. *Phys. Rev. Lett.* **98,** 260406 (2006).
30. Machida, K., Mizushima, T. & Ichioka, M. Generic phase diagram of fermion superfluids with population imbalance. *Phys. Rev. Lett.* **97,** 120407 (2006).

Supplementary Information is linked to the online version of the paper at www.nature.com/nature.

Acknowledgements We thank M. W. Zwierlein and A. Keshet for a critical reading of the manuscript. This work was supported by NSF, ONR, MURI and DARPA.

Author Information Reprints and permissions information is available at www.nature.com/reprints. Correspondence and requests for materials should be addressed to Y.S. (yishin@mit.edu).

METHODS

Phase-contrast imaging. The optical signal in the phase-contrast imaging is proportional to the net phase shift of the imaging beam passing through a Fermi mixture, that is, it is proportional to $n_\uparrow/(\nu-\nu_\uparrow^0)-n_\downarrow/(\nu-\nu_\downarrow^0)$, where ν is the probe frequency of the imaging beam, and $\nu_\uparrow{}^0$ and $\nu_\downarrow{}^0$ are the resonance frequencies of the optical transition for the states $|\uparrow\rangle$ and $|\downarrow\rangle$, respectively. When the probe beam is tuned to the middle of the two transitions, that is, to $\nu=\nu_0=(\nu_\uparrow^0+\nu_\downarrow^0)/2$, the optical signal reflects the density difference $n_\mathrm{d}=n_\uparrow-n_\downarrow$. In our experiment, two phase-contrast images of the same sample were taken consecutively with different probe frequencies, ν_1 and ν_2 (Fig. 2). The two images record the density difference $n_{\mathrm{d}1}=n_\uparrow-n_\downarrow$ and the weighted density difference $n_{\mathrm{d}2}=\alpha_\uparrow n_\uparrow-\alpha_\downarrow n_\downarrow$. The first probe frequency ν_1 was determined by zeroing the optical signal with an equal mixture and $\alpha_{\uparrow,\downarrow}$ was determined by the signal ratio between the first and the second image for a highly imbalanced Fermi mixture with $|\delta|>95\%$ (an almost fully polarized gas). Finally, we obtained $n_\uparrow=(\alpha_\downarrow n_{\mathrm{d}1}-n_{\mathrm{d}2})/(\alpha_\downarrow-\alpha_\uparrow)$ and $n_\downarrow=(\alpha_\uparrow n_{\mathrm{d}1}-n_{\mathrm{d}2})/(\alpha_\downarrow-\alpha_\uparrow)$. The difference between ν_1 and ν_2 was chosen to lie between 8 and 13 MHz.

Data analysis. Low-noise profiles were obtained by averaging the column density distribution of phase-contrast images along elliptical equipotential lines ($\lambda^2x^2+z^2=r^2$). For the measurement of the critical spin polarization, the averaging region was restricted to $|x|<12\,\mu\mathrm{m}$ to preserve the sharp features at the phase boundary. The diffraction limit for our imaging system was about 2 μm. For the determination of local quantities in the profiles, we averaged over $\pm5\,\mu\mathrm{m}$ around a given position. For temperature determination, the averaging region was restricted to an axial sector of $\pm60^\circ$ to avoid corrections due to transverse anharmonicities (see below). The relative temperature T' is determined as $T'\equiv T/T_{\mathrm{F}0}=(-6\mathrm{Li}_3(-\zeta))^{-1/3}$, where ζ is the fugacity obtained from the fit ($\mathrm{Li}_s(z)\equiv\sum_{k=1}^{\infty}z^k/k^s$ is the polylogarithmic function of order s).

Anharmonicity of the trapping potential. For the determination of temperatures from the spatial *in situ* profiles it was necessary to address the anharmonicity of the trapping potential. Our trap is generated by a weakly focused (beam waist $w\approx125\,\mu\mathrm{m}$) infrared gaussian laser beam (wavelength 1,064 nm) near the saddle point of a magnetic potential. The total trapping potential is given as

$$V(\rho,z)=U_0\exp\left(-\frac{2\rho^2}{w^2}\right)+\frac{m(2\pi f_z)^2}{2}\left(-\frac{\rho^2}{2}+z^2\right),$$

where $\rho^2=x^2+y^2$. We note that gravity has been compensated by a magnetic field gradient. The axial confinement comes mainly from the magnetic potential with oscillation frequency of $f_z=23\,\mathrm{Hz}$. The transverse magnetic potential is anti-trapping and limits the trap depth according to:

$$U=\frac{1}{4}m(2\pi f_\rho)^2w^2\left[1-\frac{f_z^2}{2f_\rho^2}\ln\left(\frac{2f_\rho^2+f_z^2}{f_z^2}\right)\right] \quad (1)$$

where f_ρ is the transverse oscillation frequency in the central harmonic region. When the trap depth is comparable to the Fermi energy of a sample, the transverse anharmonicity will affect the shape of the cloud. Although in our experiments the inner core and the outer cloud had the same aspect ratio as the trapping potential, anharmonicities were not negligible in the spatial wings used to determine the temperature.

This issue was addressed by adjusting the angular averaging region (Supplementary Fig. 3). Because the trapping potential is only anharmonic for large ρ, we could reduce the effect by decreasing the angle of the averaging sector around the axial z-direction. Both the experimental data and an exact simulation for an ideal Fermi gas show that the fitted temperature remains almost constant up to a certain angle and then increases when the averaging sector includes more of the transverse outer region. In our temperature determination, we chose the averaging sector to be $\pm60^\circ$, which was large enough to create low-noise profiles, but kept the effect of the anharmonicities to below 10%. The one-dimensional fit to angularly averaged profiles was computationally more efficient than a two-dimensional fit to a selected region of the image. In a two-dimensional fit, one could also include anharmonic terms in the fitting function.

Critical chemical potential ratio η_c. In a harmonic trap, the chemical potential of the majority and minority components are given as $\mu_\uparrow(r)=\mu_{\uparrow0}(1-r^2/R_\uparrow^2)$ and $\mu_\downarrow(r)=\mu_{\uparrow0}(\eta_0-r^2/R_\uparrow^2)$, respectively. At unitarity, the global chemical potential of a fully paired superfluid in the core is given as $\mu_{s0}=\xi\varepsilon_\mathrm{F}=\xi\hbar^2(6\pi^2n_{s0})^{2/3}/2m$ where $n_{s0}=n_{\uparrow,\downarrow}(r=0)$ is the central density. The thermodynamic equilibrium requires $\mu_{s0}=(\mu_{\uparrow0}+\mu_{\downarrow0})/2$, where $\mu_{\uparrow0}=\hbar^2(6\pi^2n_0)^{2/3}/2m$. From $\mu_{s0}/\mu_{\uparrow0}=\xi(n_{s0}/n_0)^{2/3}$, we obtain the chemical potential ratio as:

$$\eta(r)=\frac{\eta_0-r^2/R_\uparrow^2}{1-r^2/R_\uparrow^2}=2\frac{\xi(n_{s0}/n_0)^{2/3}-1}{1-r^2/R_\uparrow^2}+1$$

In our coldest sample ($\delta\approx44\%$), the normalized central density and the radius for the phase boundary were measured to be $n_{s0}/n_0=1.72(4)$ and $R_c/R_\uparrow=0.430(3)$, respectively, yielding the critical chemical potential ratio $\eta_c=\eta(R_c)\approx0.03$ with $\xi=0.42$ (ref. 11). The critical difference is $h_c/\mu=(1-\eta_c)/(1+\eta_c)\approx0.95$.